# Resonance-Based Detection of Magnetic Nanoparticles and Microbeads Using Nanopatterned Ferromagnets

Manu Sushruth, Junjia Ding, Jeremy Duczynski, Robert C. Woodward, Ryan A. Begley, Hans Fangohr, Rebecca O. Fuller, Adekunle O. Adeyeye, Mikhail Kostylev, and Peter J. Metaxas

Phys. Rev. Applied **6**, 044005 — Published 5 October 2016

DOI: 10.1103/PhysRevApplied.6.044005

# Resonance-based Detection of Magnetic Nanoparticles and Microbeads Using Nanopatterned Ferromagnets

Manu Sushruth,[1] Junjia Ding,[2,*] Jeremy Duczynski,[3] Robert C. Woodward,[1] Ryan A. Begley,[1] Hans Fangohr,[4] Rebecca O. Fuller,[3] Adekunle O. Adeyeye,[2] Mikhail Kostylev,[1] and Peter J. Metaxas[1,†]

[1]*School of Physics, M013, University of Western Australia, 35 Stirling Hwy, Crawley WA 6009, Australia.*

[2]*Department of Electrical and Computer Engineering, National University of Singapore, 4 Engineering Drive 3, Singapore 117576, Singapore*

[3]*School of Chemistry and Biochemistry, University of Western Australia, 35 Stirling Hwy, Crawley WA 6009, Australia.*

[4]*Faculty of Engineering and the Environment, University of Southampton, Southampton, SO17 1BJ, United Kingdom*

## Abstract

We demonstrate the use of nano-confined ferromagnetic resonances in periodically patterned magnetic films for the detection of adsorbed magnetic particles having diameters ranging from 6 nm to 4 $\mu$m. The nanopatterned films contain arrays of holes which appear to act as preferential adsorption sites for small particles. Hole-localized particles act in unison to shift the resonant frequencies of the patterned layer's ferromagnetic resonance modes with shift polarities determined by the localization of each mode within the nanopattern's repeating unit cell. The same polarity shifts are observed for a large range of coverages, even when quasi-continuous particle sheets form above the hole-localized particles. For large particles, preferential adsorption no longer occurs, leading to resonance shifts with polarities that are independent of the mode localization and amplitudes that are comparable to those seen in continuous layers. Indeed, for nanoparticles adsorbed onto a continuous layer, the particle-induced shift of the layer's fundamental mode is up to 10 times less than that observed in the nanopatterned systems, the low shift being induced by relatively weak fields emanating beyond the particle in the direction of the static applied field. This highlights the importance of having particles consistently positioned in the close vicinity of confined modes.

* Current address: Argonne National Laboratory, 9700 S. Cass Avenue, Argonne, IL 60439, USA

† peter.metaxas@uwa.edu.au

## I. INTRODUCTION

Magnetic biosensing techniques have shown excellent promise in terms of providing a matrix-insensitive biological detection platform for applications such as (point-of-care) medical diagnostics [1–3] and food safety monitoring [4]. These techniques center on the detection of magnetic particles which are used as tags for analytes of interest in (biological) fluids (Fig. 1(a)). Importantly, the absence of magnetic backgrounds in the majority of biological fluids enables magnetic bio-detection in minimally processed or unprocessed samples (e.g. [5–7]). While numerous methods for electronic detection of nanoparticles exist [3, 8–18], giant or tunneling magnetoresistive magnetic field sensors have garnered significant interest [1, 2, 6, 19–23]. Conventional sensing approaches using such devices are typically based on the magnetoresistive detection of magnetic-particle-induced changes to the static magnetic configuration within the device (Fig. 1(b)) [24]. Thus, like Hall effect sensors [14, 15, 25], they offer a sensing method based on detecting changes to a (potentially modulated) d.c. voltage level.

However, it is also possible to exploit the magnetic field dependence of resonant magnetization dynamics for particle sensing [26–31]. The field dependence of these dynamics mean that the precession frequency of the magnetization (which is typically in the gigahertz range), will be altered by particle-generated magnetic fields (Fig. 1(c)). This opens the way for an intrinsically frequency-based, rather than amplitude-based, sensing technique [26, 32]. One potential advantage of this technique is that the stray magnetic fields generated by the particles act directly on the precessing moments, avoiding magnetoresistive sensing's requirement to detect particle-induced changes to the magnetic configuration of the system [31]. The consequence of this is that resonance-based sensing can be carried out at large external fields where particle-generated fields are maximized (i.e. sensing can be realized even when the sensor's magnetic state is saturated and therefore insensitive to small changes in the local field) [31, 33]. Furthermore, the use of spin torque oscillators [26, 32] enables electrical read out of the resonant magnetization dynamics in real time [34–37], potentially enabling high speed sensing with sub-100 nm devices [26] for applications such as cytometry [25, 38–40]. Note that one of the resonant modes used here for particle detection is confined laterally to a region with size on the order of $100 \times 100$ nm$^2$.

This work will focus on magnonic crystals (MCs) which are attractive systems to explore

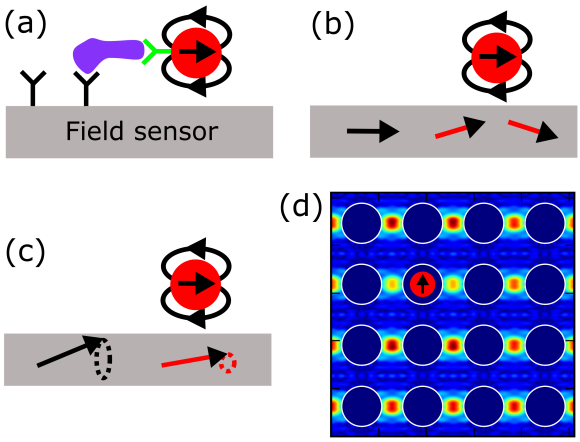


FIG. 1. (a) Schematic of a sandwich immunoassay showing a magnetically labeled biological entity specifically bound to a chemically functionalized sensor. The nanoparticle stray field can induce changes to the (b) static magnetization configuration of a ferromagnetic sensing element or (c) its precessional magnetization dynamics. (d) Shows a spherical magnetic nanoparticle (red) within a hole (white circles) in a hole-based, periodic magnonic crystal with geometry equivalent to that studied in Sec. 2.2 (300 nm wide holes). Both the particle and patterned film are magnetized towards the top of the page. The particle stray field locally modifies the amplitude of precessional magnetization dynamics around it. The dynamics correspond to a side mode resonance which is localized between the holes. The color encodes the amplitude of the magnetization precession in the magnetic layer (red = high; blue = low). Except for the single nanoparticle, there is no magnetic material within the holes.

the fundamentals of a resonance-based sensing technique for magnetic (nano)particles. MCs are magnetic materials which have been artificially patterned (typically at the nanoscale) to control spin-wave (magnon) propagation or enable periodic confinement of nano-localized ferromagnetic resonances [41] (e.g. Fig. 1(d)). High levels of periodicity over large length scales mean that these systems' localized resonant modes (analogous to those excited in isolated nanostructures) can be probed easily in laboratory settings in macroscopic samples (e.g. [42]). Beyond envisioned applications in data and signal processing (e.g. [43]), we have previously demonstrated that MCs can be used to understand the influence of magnetic fields generated by magnetic nanoparticles on highly localized ('spatially confined') ferromagnetic resonance [30]. Notably, using a hole-based structure enables the localization of particles

within the holes with a subsequent predictable local modification of the resonant precession of the magnetization in the neighborhood of the captured particle. An example of this can be seen in Fig. 1(d) as a change in the color-coded precession amplitude to the left and right of the hole-localized nanoparticle. More recently, similar effects were confirmed numerically in another hole-based MC geometry [44].

In this paper we demonstrate the successful use of nano-localized ferromagnetic resonance (FMR) modes for the detection of magnetic particles with a range of diameters spanning 3 orders of magnitude: from sub-10 nm superparamagnetic iron-oxide nanoparticles to 4 $\mu$m wide beads. This particle size range also approximates a correspondingly large range of biological length scales, from single proteins [45, 46] to exosomes [47] and cells [18, 25]. We will explicitly show the advantage of using hole based structures for the localization of both modes and particles, the latter ensuring a common, and thus reinforcing effect, from individual particles. Indeed we show that the sensitivity can be an order of magnitude less when using an unpatterned (i.e. continuous) ferromagnetic layer. There, the dominant effect is from the stray field extending far outside the particles which is weak compared to that beneath or directly neighboring each particle.

For nanoparticles within a nanopatterned MC's holes however, the localization of different modes in the regions direcly surrounding each hole can lead to large shifts with the mode localization defining the sign of the frequency shift. This shift polarity is maintained and its amplitude increased at high particle coverages where quasi-continuous sheets of particles form. However by increasing the particle size to a degree in which the particle cannot enter the holes, we lose the mode-dependent shift polarities with all modes behaving similar to the fundamental mode of a continuous layer in that their frequencies all increase. Varying the particle size can thus enable a transition to film-like sensing behavior, albeit with multiple modes existing in the patterned MC. Note that all particles studied in this work exhibit a quasi-null magnetic moment in zero field (as checked via magnetometry) and thus minimal agglomeration.

## II. METHODS

### A. Experimental details

The nanopatterned films studied here consist of square arrays of circular holes ('anti-dots') in a 30 nm thick Permalloy ($Ni_{80}Fe_{20}$) film with a 8 or 10 nm gold (Au) capping layer. The array pitch is 450 nm with hole diameters of 240 nm or 300 nm. The large area ($4 \times 4$ mm$^2$) MCs were fabricated on silicon (Si) substrates using deep ultraviolet lithography, e-beam deposition and liftoff [48]. The continuous layer studied in Sec. III A has the same composition as the MCs.

FMR measurements of the continuous films and nanopatterned MCs were obtained using broadband microwave stripline-based FMR spectroscopy (e.g. [49]), a technique where resonant magnetization dynamics are excited in magnetic materials using a radio-frequency (r.f.) field, here generated by an r.f. signal passing through an underlying stripline. An absorption of microwave power by the magnetic sample is measured when the frequency of the r.f. field matches that of a FMR mode. Here we used field-modulated FMR spectroscopy wherein a lock-in amplifier measures the external field-($H_{\text{ext}}$-)derivative of the FMR response at a constant frequency while sweeping $H_{\text{ext}}$ using an electromagnet. An interferometric receiver was used to maximize signal amplitudes [50]. This is particularly important in our measurement since the sample is separated from the stripline by a microscope coverslip (rather than sitting directly on the stripline). The coverslip ensures that particles do not rub off onto the micro-stripline but reduces the signal amplitude. $H_{\text{ext}}$ was measured with a Teslameter (FH 54; Magnet-Physik Dr. Steingroever GmbH) and typically swept between $\sim 0$ and 350 mT. We note that an overall decrease in the differential FMR signal was seen when adding increasing concentrations of particles. To enable comparison of traces, the traces were vertically scaled. A small vertical offset (a few tens of $\mu$V at most) also had to be corrected for in some cases.

Particle detection was carried out for a range of particles with average or supplier-stated diameters of 6 nm, 50 nm, 130 nm, 880 nm and 4.14 $\mu$m (see Appendix A for further details). Particles were applied in solution to the upper surface of the film or MC in ambient laboratory conditions in the absence of an external magnetic field ($H_{\text{ext}} = 0$). The solutions were then allowed to dry before (a) imaging the particle-covered film or MC via scanning

electron microscopy and (b) remeasuring the FMR traces.

### B. Micromagnetic simulations

Micromagnetic simulations were carried out to predict field-dependent FMR mode frequencies and spatial profiles of the FMR modes. They were run for a single unit cell ($450 \times 450$ nm$^2$) of the MC's hole array or an equivalently sized region of continuous film. We employed periodic boundary conditions and a tiled macrogeometry [51] ($33 \times 33$ unit cells). The following parameters were used for the patterned MC and the unpatterned films: damping $\alpha = 0.008$, nil intrinsic anisotropy, gyromagnetic ratio $2\pi\gamma = 1.85 \times 10^{11}$ rad/T.s, saturation magnetization $M_S = 8 \times 10^5$ A/m and exchange stiffness $A_{ex} = 13$ pJ/m.

Micromagnetic simulations will be used used to determine the effect of 130 nm wide nanoparticles on the FMR modes. For such simulations, the simulation region was extended vertically to enable us to explicitly include discretized spherical nanoparticles within the simulation's macro-geometry. Note that although the supplier-provided nanoparticle size is 130 nm, we used a width of 150 nm in the simulations as in [30]. For nanoparticles lying within the holes of the patterned layer, the lower surface of the spherical particle was always aligned with the lower surface of the magnetic layer (i.e. resting on the underlying Si wafer). For particles on top of the ferromagnetic layer's surface, the lower surface of the particle was set at 10 nm above the upper surface of the magnetic layer (i.e. sitting on the upper surface of the non-magnetic capping layer). For the simulation, nanoparticles were treated as ferromagnets with damping $\alpha = 0.05$, gyromagnetic ratio $\gamma$ as above and a $H_{\text{ext}}$-dependent $M_S$ taken from magnetometry measurements of freeze dried nanoparticles [30].

MuMax3 [52] was used to obtain the presented micromagnetic simulation results. The system was first initialized with a uniform magnetization in the (0.5,1) direction and allowed to relax in the presence of an external field (applied along the $y$-axis) using MuMax3's internal relaxation routine. Post-relaxation, an excitation sinc pulse of 0.5mT (cut-off freq 30 Ghz, 300 ps offset) was applied along the $x$-axis to induce broadband, precessional magnetization dynamics. The resultant damped ringdown of the spatially averaged $x$-component of the magnetization, $m_x$ (recorded in the time domain), was then Fourier analyzed. All resultant mode profile visualizations were determined by extracting the spatially resolved $m_x$ Fourier amplitudes at each identified resonant frequency across the simulation region.

Obtained results are shown as intensity plots with the brightest regions corresponding to the highest Fourier amplitude for $m_x$ at that frequency (see for example the insets in Fig. 2(a)). The Matplotlib, NumPy and SciPy [53, 54] packages were used for analysis and visualization of the simulation data. The eigensolver (see e.g. [31, 55]) in the FinMag micromagnetic simulation package (based on Nmag [56]) was also used for some test cases with good levels of agreement [30] (e.g. Supplementary Figure 1 [57]).

## III. RESULTS AND DISCUSSION

### A. Continuous layers

We first consider the case of particle-induced shifts of the fundamental FMR mode in continuous, *unpatterned* magnetic layers where, in the absence of particles, resonant dynamics will typically be laterally uniform across the layer. Fig. 2(a) shows a schematic of the dipole field of a magnetic particle acting on an underlying magnetic film subject to an external in-plane static field, $H_{\text{ext}}$. The in-plane component of the particle's field, $H_{\text{P}}$, is strong and opposes $H_{\text{ext}}$ directly below the particle [in region '2', Fig. 2(a)] and to the sides of the particle, the latter due to the symmetry of the dipolar $H_{\text{P}}$. Elsewhere [regions '1' and '3', Fig. 2(a)], the in-plane component of $H_{\text{P}}$ is weaker but reinforces $H_{\text{ext}}$. Subsequently, although a bare, thin magnetic layer has one primary resonance mode (which corresponds to the spatially uniform fundamental mode, shown as a solid line in Fig. 2(b)), an additional, low frequency mode appears in simulation when isolated particles are on top of the film.

The low frequency mode is located beneath the particle and to its sides where $H_{\text{P}}$ opposes $H_{\text{ext}}$ (see bottom left inset in Fig. 2(b) while comparing to region '2' in Fig. 2(a)). Since the total field is reduced at that position, so is the resonance frequency. The majority of the dynamics within the layer are however concentrated in the remainder of the simulation region, as seen in the bottom right inset of Fig. 2(b) (these areas correspond to regions '1' and '3' in Fig. 2(a)). This mode is slightly upshifted in frequency [Fig. 2(b)] due to the weak $H_{\text{P}}$ in those regions reinforcing $H_{\text{ext}}$ which increases the total field. Notably, at a particle-layer separation of 10 nm, the maximum in-plane $H_{\text{P}}$ directly below a single, perfectly spherical particle will be approximately 15 times higher than the maximum in-plane $H_{\text{P}}$ at the upper/lower boundaries of the computation cell. This explains the disparity in the shift

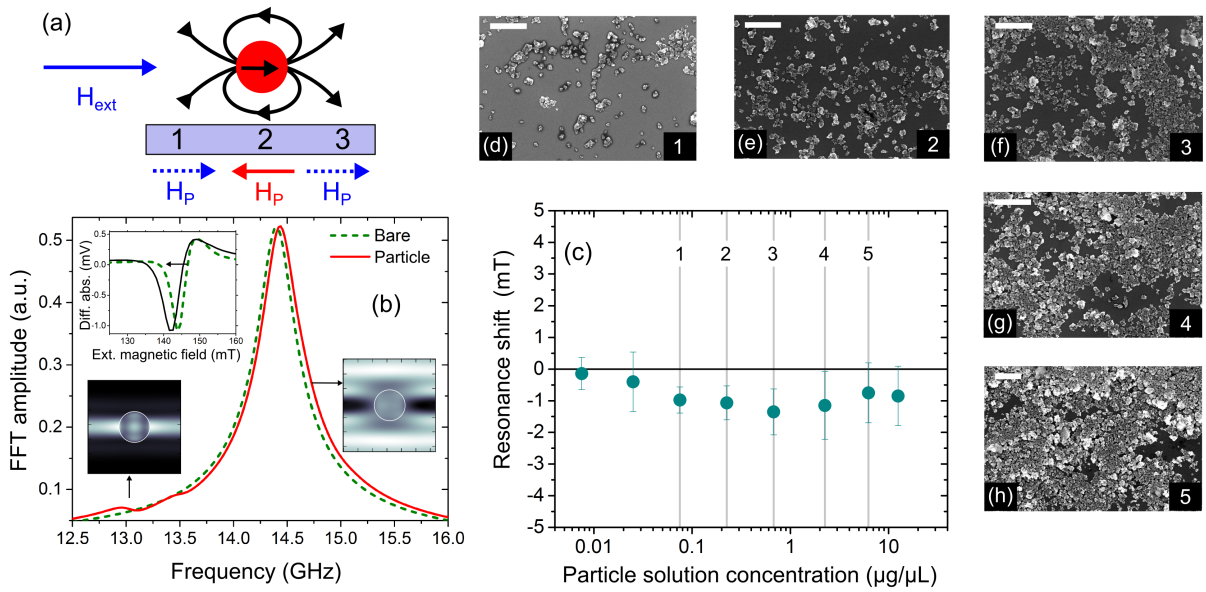


FIG. 2. (a) Schematic side view of a particle placed on an underlying magnetic film. The in-plane stray magnetic field generated by a particle, $H_{\mathrm{P}}$, is strong and opposes the applied in-plane static field ($H_{\mathrm{ext}}$) directly below it, resulting in a strong downward shift in the resonance frequency in that region (marked as '2'). In regions '1' and '3', $H_{\mathrm{P}}$ is weaker (blue dashed lines) but reinforces $H_{\mathrm{ext}}$, thus slightly increasing the resonance frequency. (b) Fourier transformed time domain simulation data for an un-patterned film showing a small upward shift in fundamental mode's frequency in presence of a particle. The upper-left inset shows experimental FMR traces, obtained at 12 GHz, with (solid black line) and without (dotted green line) particles (concentration is 0.675 $\mu$g.$\mu$L$^{-1}$) on the surface of unpatterned film. Lower insets show the simulated mode profiles of the two main modes that exist in the presence of a particle. (c) Experimentally obtained result for fundamental mode shifts of an unpatterned film as a function of particle concentrations. The measured shifts for each concentration are the average shift for frequencies ranging 11.5 - 16 GHz. (d-e) SEM images showing the distribution of particles on the unpatterned film's upper surface. White scale bars are 1 $\mu$m long.

amplitudes seen for the dynamics concentrated in region '2' versus those concentrated in regions '1' and '3'.

In a field-resolved experimental FMR trace (obtained at a fixed frequency, upper-left inset of Fig. 2(b)), the predicted particle-induced frequency upshift of the fundamental mode manifests as a downshifted resonance field. This is due to the reinforcing effect of $H_p$ which

reduces the magnitude of the external field that must be applied to meet the resonance condition. In Fig. 2(c) we show the consistently negative experimentally observed shift of the fundamental resonance for increasing particle coverages. Different particle coverages were obtained by applying consecutively higher concentrations of particle-containing solutions to the film and measuring the FMR spectra between each application. Note that the shift is highest for intermediate particle coverages (Figs. 2(f-g)) where there are large numbers of isolated particles or clusters of particles on top of the layer. As expected, low particle coverages (Figs. 2(d-e)) lead to a low reinforcing $H_{\mathrm{P}}$ when averaged across the film and thus a low shift. At high coverages however, quasi-continuous particle layers form which also generate relatively small shifts. This is likely because the particle sheets approximate continuous layers which, ignoring effects of roughness and lateral boundaries, generate negligible stray fields.

The average resonance frequency shift obtained from the simulation (Sec. II B) is 34 MHz ($\equiv 0.7$ mT given an experimentally measured slope of 49.4 GHz/T for the fundamental mode, see Supplementary Figure 2 [57]). This is comparable to the maximum experimentally observed field shift in the continuous layer ($1.3 \pm 0.7$ mT). Thus, we can conclude that the weak shift observed for the continuous layer is not a result of an intrinsically low field sensitivity of the resonance. In fact, it is actually quite high at almost 50 GHz/T. Rather, the weak shift is due to the dominant FMR signal coming from portions of the film subject to the relatively weak reinforcing $H_{\mathrm{P}}$ fields that surround the particles (i.e. regions '1' and '3' in Fig. 2(a)) instead of the more intense $H_{\mathrm{P}}$ fields located directly beneath the particles.

### B. Patterned films: hole arrays

We now turn to the nano-patterned MCs for which it is possible to have spatially localized resonances in regions where $H_{\mathrm{P}}$ is large. The main panel of Fig. 3(a) shows a simulated ferromagnetic resonance spectrum at $H_{\mathrm{ext}} = 180$ mT for a MC with 300 nm wide holes on a 450 nm square lattice. The excitation spectrum is clearly much richer than the continuous layer with a number of modes, each having different localizations within the unit cell (Fig. 3(b)). The simulated traces have been differentiated with respect to frequency for more natural comparison to experimental FMR traces. We will focus predominantly on the side mode (SM, shown also in Fig. 1(d)) and extended mode (EM) with intermediate (IM)

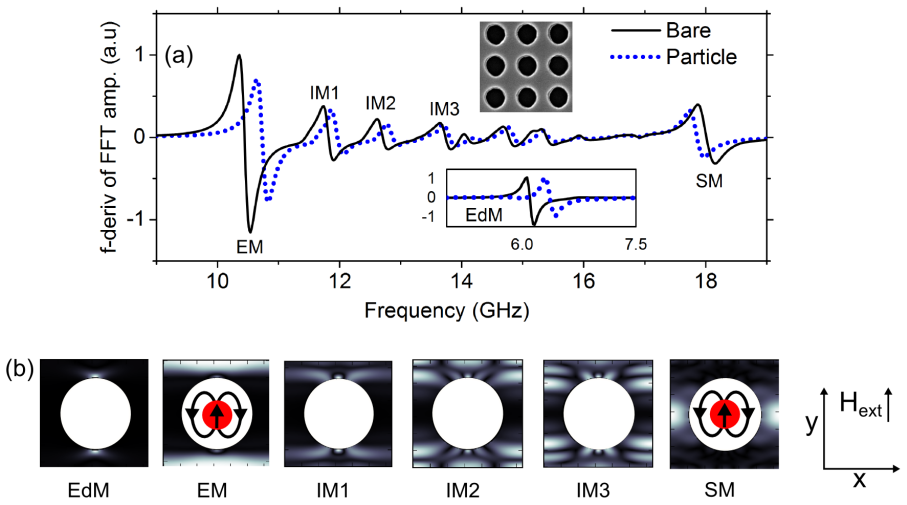


FIG. 3. (a) Simulated frequency resolved FMR spectra obtained at $H_{\text{ext}} = 180$ mT applied in y-direction for a 300 nm MC with (dotted blue lines) and without (solid black line) a particle inside the hole. The upper inset shows an SEM image (1.3 $\mu$m x 1.3 $\mu$m ) of the MC and the lower inset shows the simulated resonance shift of the EdM in the presence of a particle. (b) Spatial concentration of dynamics for a number of resonance modes within a unit cell of the MC. A schematic of a particle and its stray field has been added to the EM and SM profiles.

and edge modes (EdM) discussed only briefly. While the SM is largely localized between horizontally neighboring holes, the EM occurs over extended bands running between rows of holes orthogonal to the applied field (Fig. 3(b)). IM1-3 have similar localizations to that of the EM. Good agreement is found between the simulation and experiment for both the overall mode spectrum and the frequencies of the EM and SM (Supplementary Figure 3 [57]).

Depending on the spatial localization of each mode, the stray magnetic field from magnetized particles within the holes has a $y-$component which can locally reinforce or oppose the $y-$oriented external field [30, 58]. This is shown schematically for the SM and EM in Fig. 3(b) (one can consider the more localized modes as being nano-scale dynamic probes for the particle stray fields). Since the $y-$component of $H_{\text{P}}$ opposes $H_{\text{ext}}$ where the SM is localized, the mode's frequency reduces due to a reduced net field at that location. This is seen in Fig. 3(a) where we have also included the simulated resonance spectrum in the presence of a 150 nm wide particle at the lateral center of the simulation region's anti-dot. In contrast, the EM (and EdM) resonances shift upwards in frequency since $H_{\text{P}}$ reinforces

$H_{\text{ext}}$ at the upper/lower parts of the unit cell. Note that the confinement of the modes in well-defined regions close to the particle where the stray fields are strong (i.e. directly to the sides of the particle ($\pm x$) and directly in front of/behind it ($\pm y$)) mean that significant shifts are induced for both the EM and SM ($\sim 0.1 - 0.3$ GHz: $\sim 10$ times larger than that observed for the continuous layer). This is despite the sensitivities of the MC's EM and SM to static, uniform external fields being comparable to that of the continuous layer's fundamental mode. The EdM and IMs are also subject to clear positive shifts in the presence of a hole-localized particle, consistent with the fact that they, like the EM, have their dynamics concentrated in the upper/lower portions of the unit cell (i.e. also subject to $H_{\text{P}} > 0$).

Following the same protocol as for the continuous layer in the previous section, we measured the SM and EM shifts versus particle concentration experimentally in a 300 nm MC (i.e. an MC with 300 nm wide holes). The EM resonance field decreases since $H_{\text{P}}$ locally increases the magnetic field (Fig. 4(a)). The consequence of this is that the resonance can be attained experimentally at a lower $H_{\text{ext}}$ at each microwave frequency. The resonance fields of IM1-3, which have an EM-like localization, also shift downward in experiment (Supplementary Figure 4 [57]). In contrast, the SM resonance field increases because $H_{\text{P}}$ locally shields the SM from $H_{\text{ext}}$ (Fig. 4b). This means that a larger $H_{\text{ext}}$ must be applied to attain the resonance condition. These shift directions are consistent with those seen in the frequency-resolved simulation data [Fig. 3(a)]. Quantitative comparisons of the measured and simulated shifts are made below.

As seen previously for low coverages [30], we observe a continuing increase of the shift magnitudes with particle coverage over a very wide range of coverages (Fig. 4(c)). For lower nanoparticle solution concentrations, the majority of particles are found within the holes (Figs. 4(d,e)) with both the percentage of filled holes and the percentage of particles lying within the holes increasing with the concentration of the applied particle solution (Supplementary Figure 5 [57]). Saturation of the shifts commences at the penultimate concentration where a quasi-continuous layer of particles form (Figs. 4(g,h)). Notably, the maximum shifts in the MC are, as expected from simulation, significantly higher (up to $10\times$) than the maximum shift observed in the continuous layer. Note that the continuous layer data from Fig. 2(c) has been plotted with the MC data in Fig. 4(c) to enable direct comparison. Another point to note is that while the continuous layer resonance field shifts decrease when a quasi-continuous particle sheet forms, in the MC, sheet formation increases

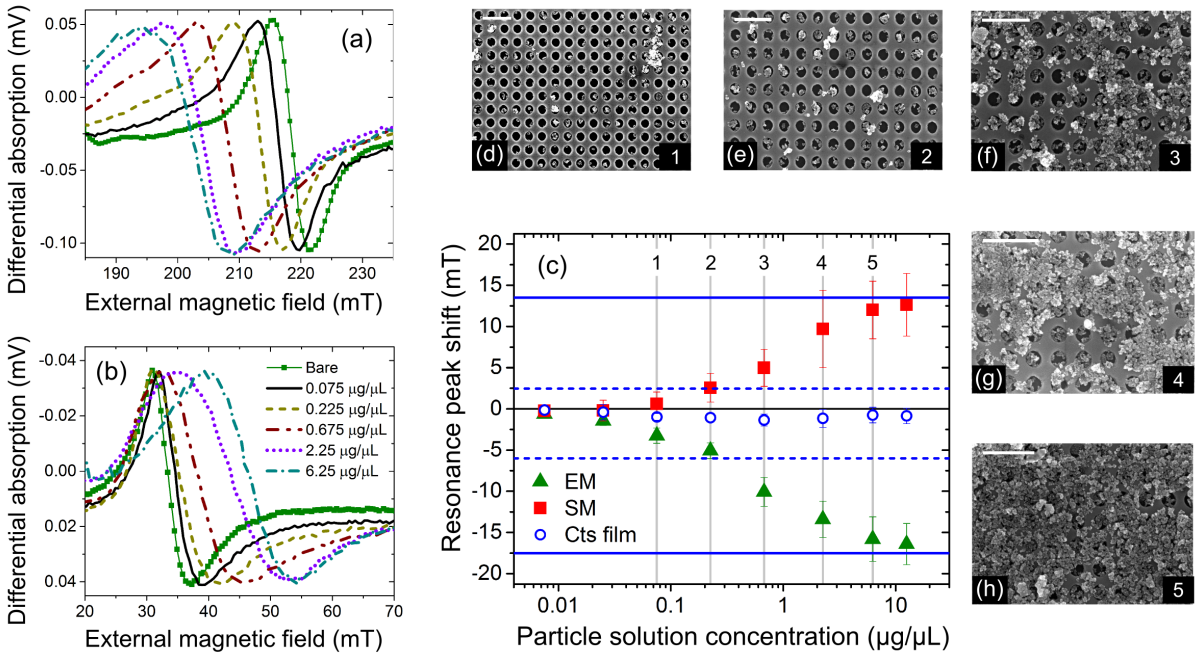


FIG. 4. Experimental FMR traces (obtained at 12 GHz) showing shifts in (a) EM and (b) SM resonance lines with increase in particle concentration.(c) Experimentally obtained result for EM and SM resonant shifts for a 300 nm MC as a function of particle concentrations. Horizontal (dashed) lines show the simulated EM and SM resonant shifts for (1 particle/hole) a 150 nm thick sheet of particles on the surface. The error bars are a measure of the spread of shifts across the measured frequency range (11.5 - 16 GHz) and also includes the uncertainties related to slight variations in sample placement ($\sim 0.5$ mT at most). The continuous film's fundamental mode shift versus particle concentration (Fig. 2c) is plotted (blue open circles) for direct comparison with the patterned film. (d-h) SEM images showing clustered shaped nanoparticles inside holes and on the upper surface of the MC. White scale bars are 1 $\mu$m long. The first four data points for the EM and SM in (c) as well as the bare and 2 lowest concentration traces in (a) have been presented previously [30].

the observed shifts, an effect which is reproduced below via simulation.

We now discuss the reproduction of the observed shifts for the EM and SM (Fig. 4(c)) at the two coverages which can be most easily simulated. The first coverage is that obtained for 0.225 $\mu$g/$\mu$L, where there is approximately 1 particle in each hole [Fig. 4(e)]. There, simulations were carried out by adding a 150 nm wide particle to the simulation at the hole center (as already described in Sec. II B) and observing the resultant shifts in the

FMR mode frequencies. For the high coverage scenario, we replaced the particle with a disk (diameter 40 nm less than the hole diameter) which was covered by a contiguous 150 nm thick continuous layer. This 'disk+layer' had the same magnetic properties as the spherical particles (Sec. II B). It successfully approximated the high particle coverage scenario (Figs. 4(g,h)) where the filled holes are covered by a semi-complete particle sheet. The resultant simulated shifts, converted from frequency shifts to field shifts using the data in Supplementary Figure 3(a) [57], are shown in Fig. 4(c). There we show the simulated shifts for the EM and SM for one particle per hole (horizontal dashed line) and full particle coverage (solid dashed line). There is excellent agreement between these values and the shifts experimentally obtained, respectively, at the fourth and final coverages.

The simulated and experimental FMR resonance field shifts given above are the average of the shifts obtained at the different r.f. frequencies used in the experiment (11.5 GHz - 16 GHz). When we change the r.f. frequency however, we change the resonance field for each mode [as per Supplementary Figure 3(a) [57]] and this enables a measurement of the field-dependence of the nanoparticle-induced FMR resonance field shift. At low $H_{\text{ext}}$ for example, the magnetization of the particles is reduced and this subsequently reduces the shift observed for the SM (note that only the SM can be measured at low field for our frequency range). This reduced shift can be seen in Fig. 5 with good agreement between simulation and experiment: experimental data has been obtained at 0.225 $\mu$g/$\mu$L with the simulated shifts obtained under the assumption of 1 nanoparticle per hole (as above). The simulations take into account the field-dependent moment of the particle, also given in Fig. 5. The resonance field shift is found to follow the $H_{\text{ext}}$-dependent particle moment quite closely, approaching saturation at high field. This highlights the ability to carry out resonance-based sensing even at high fields [31] where nanoparticle moments can be maximized. Field dependent experimental resonance field shifts for the SM and EM at all coverages together with simulation results are shown in Supplementary Figure 6 [57] (up to $H_{\text{ext}} = 320$ mT for the EM).

We finally note that particle sensing was also demonstrated with a second MC having smaller holes (240 nm) but the same lattice pitch. Analogous effects were observed except that the shifts were reduced. The shifts could albeit be reproduced by assuming a filling proportional to the hole size (Supplementary Figure 7 [57]). This is consistent with the reduced shifts being due to a reduced capability of filling rather than an intrinsically lower

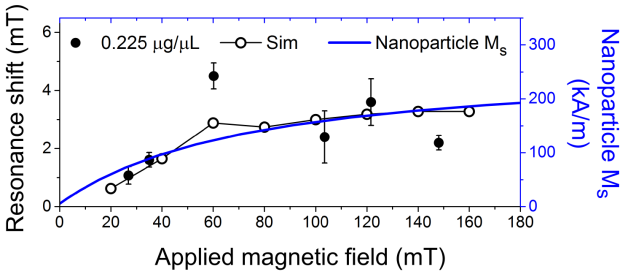


FIG. 5. Left axis: Resonance field shift versus external applied field for the SM in the 300 nm MC at 0.225 $\mu$g/$\mu$L together with simulated SM mode shifts for the case of one particle/hole. The simulated frequency shifts obtained were converted to fields using the data in Supplementary Figure 3(a) [57]. Right axis: 130nm particle magnetization per unit volume at 300 K (measured using SQuID magnetometry; data previously published in [30]).

field sensitivity of the modes. Indeed the intrinsic field sensitivities are comparable to those for to the MC with 300 nm holes [Supplementary Figures 3(a,c) [57]].

### C. The role of particle size and localization

In Figs. 6(a-d), we show shifts in the EM resonance field induced by particles with different diameters: 6 nm, 50 nm, 0.88 $\mu$m and 4.14 $\mu$m. Clear shifts are observed in all cases, demonstrating the compatibility of this sensing method with a very large range of particle sizes. As explained below however, the polarities of the observed shifts depends on the size of the particles relative to the size of the holes. Before concentrating on the shift polarities, we briefly note that, as seen in Figs. 4(a,b) and 6(a-d), the dominant effect of both nanoparticles and beads is typically a resonance shift, albeit accompanied by a relatively weak degree of linewidth broadening. Exceptions to this are the 0.88 $\mu$m particles and the highest coverage scenario for the 6 nm particles where broadening and shifts are comparable.

The opposite SM and EM shift polarities seen in Fig. 4(c) for the 130 nm particles were observed for two other particle types, the common aspect of these particles being that they could enter the MC's holes due to their small size: 6 nm wide particles (Fig. 6(a) and Supplementary Figure 8 [57]) and 50 nm wide particles (Figs. 6(b,e-g)). In both cases, the overall trend, as for the 130 nm particles, is again a stronger shift with increasing particle coverage. This is seen clearly in Figs. 6(a,b) showing consecutively larger shifts of the EM

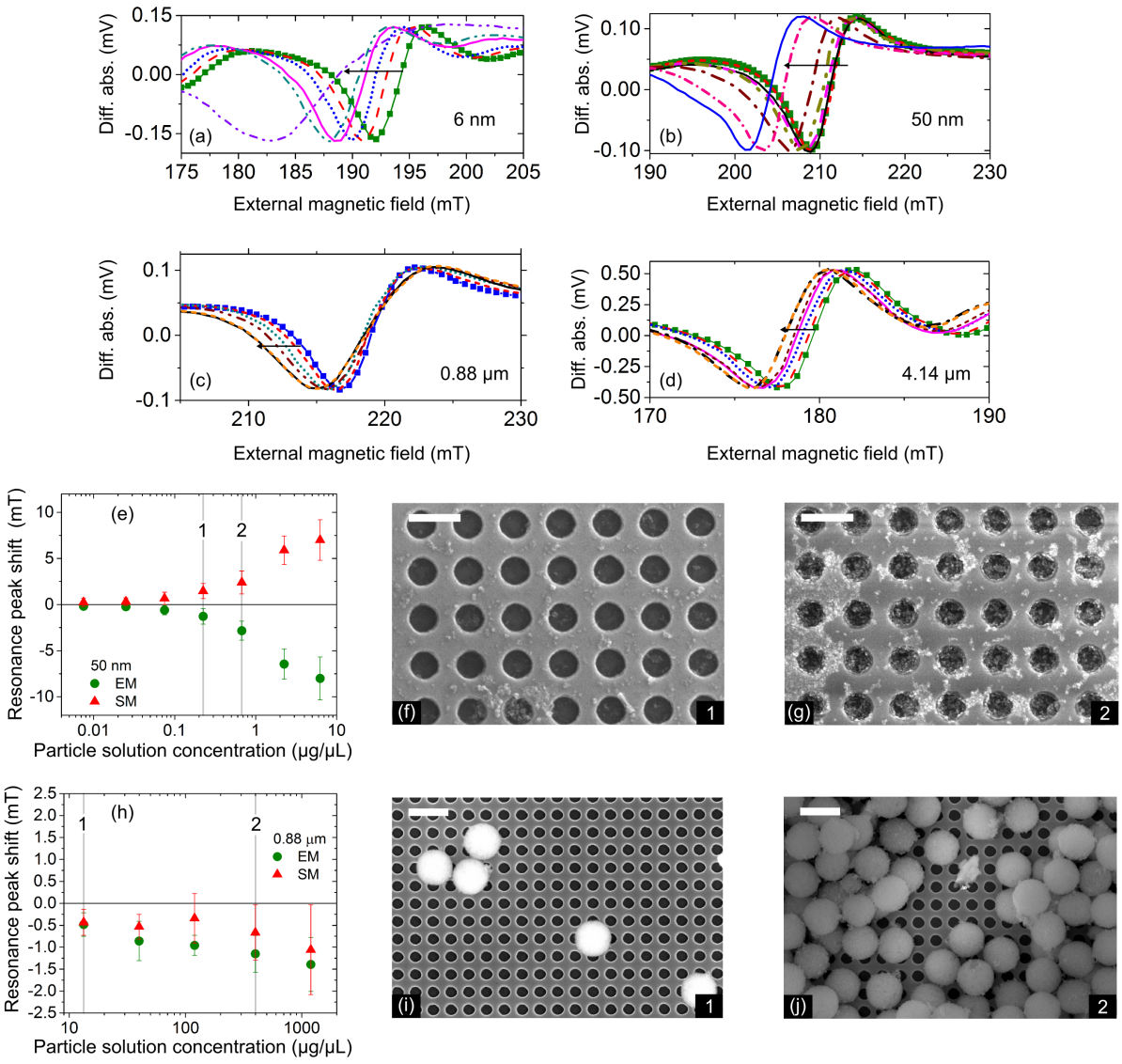


FIG. 6. Experimentally obtained EM FMR traces (excited at 12 GHz) showing decrease in resonance field with increase in concentration of (a) 6 nm nanoparticles, (b) 50 nm nanoparticles, (c) 0.88 $\mu$m magnetic beads and (d) 4.14 $\mu$m magnetic beads. (e) EM and SM resonant shifts as a function of applied 50 nm particle concentrations. SEM images showing the distribution of 50 nm particles for (f) lower and (g) higher concentrations. (h) EM and SM resonant shifts as a function of applied 0.88 $\mu$m bead concentrations. SEM images showing the distribution of 0.88 $\mu$m wide magnetic beads for (i) lower and (j) higher concentrations. The error bars in (e,h) are a measure of the spread of shifts across the measured frequency range (11.5 - 16 GHz). White scale bars are 1 $\mu$m long.

resonance for both particle sizes. Note that a clear SM shift was seen for the 6 nm particles only at the highest concentration (Supplementary Figure 8 [57]).

For particles with diameters that are larger than the hole diameter, both the SM and EM are characterized by negative polarity field shifts. The relevant data is shown in Fig. 6(c,h-j) (0.88 $\mu$m beads) and Fig. 6(d) (4.14 $\mu$m beads, see also Supplementary Figure 8 [57]). This mirrors the behavior observed for the fundamental FMR mode in the continuous, unpatterned layer in the presence of 130 nm wide nanoparticles. This suggests that for large particles which are not predominantly hole-localized, the dominant shift, as for the continuous layer, comes from in-plane fields which are generated by surface-located beads and which reinforce $H_{\text{ext}}$. Note that although there is some centering of the 0.88 $\mu$m particles on top of holes observed at low concentrations (two bottom right particles in Fig. 6(i)), the larger particles are typically randomly distributed across the MC. As a result, for purely surface-located beads, both the EM and SM shift in the same direction since they are, when taking a macroscopic average over the sample, subject to equivalent parts of the particle-generated field profiles.

Note however that even with the *nano*particles, significant numbers of isolated particles or groups of particles also can be surface-located. This has already been highlighted for the 130 nm particles [Fig. 4] and can be seen clearly in Fig. 6(g) for the 50 nm particles. The shifts induced by surface-located nanoparticles has been calculated via simulation for three different surface positions [scenarios II-IV in Fig. 7(a)] where simulated shifts of the SM and EM due to surface-located particles are compared to the shifts induced by a particle at the center of the hole [scenario I in Fig. 7(a)]. The shifts, measured relative to the FMR frequency for a bare MC, are given in Figs. 7(b,c).

When a particle is directly above the position where a mode's dynamics are concentrated, it can generate a resonance shift which is larger than that observed for hole-localized nanoparticles. Indeed, due to geometrical confinement of FMR modes in the MC, the whole region containing the mode can be subject to the strong $H_{\text{P}}$ below a particle. This field opposes $H_{\text{ext}}$ and is thus capable of strongly decreasing the resonance frequency of that mode. These strong reductions in the frequency are marked with asterisks in Fig. 7(b,c). They occur for the SM in scenario II where the particle lies directly above the region where the SM is localized and for the EM in scenarios III and IV where the particle lies at points that are directly above the EM excitation band. When the EM or SM resonance frequency is strongly

downshifted, the other mode experiences a weaker upshift, since the other mode's dynamics will be located at a region where $H_{\mathrm{P}}$ is weak but reinforces $H_{\mathrm{ext}}$, thus increasing the FMR frequency [equivalent to regions '1' and '3' in Fig. 2(a)]. The critical point here though is that the placement of small particles on the MC's upper surface is quite random within the unit cell. As a result, and as observed in experiment, the resonance shifts observed for the macroscopic MC are dominated by those induced by the hole-localized particles, even though the shifts induced locally by individual surface-located particles can be high with position-dependent polarities.

In the experiments carried out with 130 nm particles, most particles are hole-localized at low coverages and thus have a dominating effect on the modes (i.e. frequency downshifting for the SM and upshifting for the EM). At the other extreme (i.e. for high coverages), sheets form and, as already shown, the change is such that it reinforces the effect of hole-localized nanoparticles [Fig. 4(c)]. At intermediate coverages however there is a large number of isolated particles (or groups of particles) on the MC's upper surface (e.g. the 5th highest concentration; Fig. 4(f)). It is around this concentration where we see a maximum in the linewidth broadening - the linwidth has been plotted versus particle concentration in Fig. 7(d). This maximum broadening is consistent with a high number of surface-located particles (depending on their quasi-random positioning, their presence can both increase or decrease the resonant fields). For a collection of surface-located nanoparticles, this will broaden the resonance linewidth by generating localized upshifting and downshifting across the macroscopic MC. The formation of a quasi-continuous layer of particles at higher coverages however, would be expected to reduce the strong localized fields generated underneath the particles. Indeed, at these higher coverages, there is a slight reduction of the linewidth (Fig. 7(d)) consistent with a reduced contribution from isolated surface-located particles. We also note that distributions in the particle sizes (as can be identified in Figs. 4(d-h)) will contribute to linewidth broadening since smaller (larger) particles will generate smaller (larger) shifts (Supplementary Figure 9 [57]). This broadening will be in a common direction however since both smaller and larger hole-localized particles generate shifts of the polarity shift.

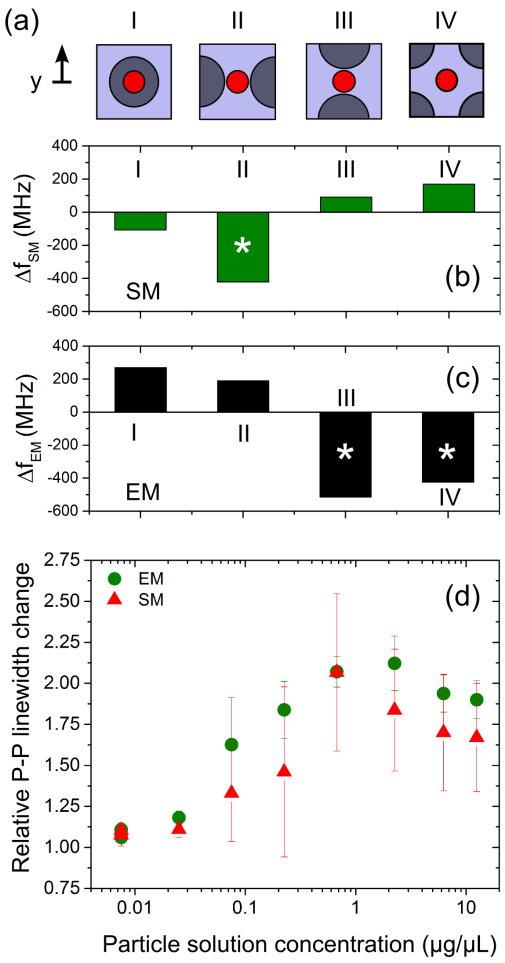


FIG. 7. (a) Schematic showing the particle positions with respect to the MC hole. Simulated (b) SM and (c) EM frequency shifts measured with respect to the bare frequency for a 150 nm particle located within the MC hole (I) and at various positions on the MC surface (II: above the SM region; III, IV: above the EM region). Significant reductions in a mode's frequency (marked with an asterisk) are observed when a particle is above the region of the MC containing that mode. (d) Experimentally observed changes in EM and SM resonance linewidths as a function of 130 nm particle concentrations applied to 300 nm MC. The error bars are a measure of the spread of linewidth broadening across the measured frequency range, 11.5 - 16 GHz. Data for the lowest four concentrations are taken from [30].

## IV. CONCLUSION

We have demonstrated the use of nano-confined ferromagnetic resonance modes in nanopatterned magnetic layers for sensing a wide range of magnetic particle sizes. This

has been motivated by the potential for the development of frequency-based (rather than voltage-based) sensing methods for use in magnetic biosensing. Resonance-based particle detection has been carried out for magnetic particles with sizes from 6 nm to 4 $\mu$m. The particles' stray magnetic fields act directly on the precessing moments within the magnetic layers, generating significant shifts in the resonance fields (or, equivalently, the resonant frequencies). Thanks to this direct action, the observed resonance shifts in our hole-based patterned ferromagnet can be maintained over large ranges of fields, meaning that resonance-based nanoparticle detection can be used at high field where particle moments (and thus particle-generated fields) can be maximized. The dominant effect of the particles is typically a resonance shift rather than a broadening of the resonance linewidth, a result which is encouraging for the future implementation of a sensing method based on sensitively detecting changes to resonance frequencies.

In this work, we also identified different characteristics in the resonance shifts for small and large particles. For small particles, their preferential capture in our system's nano-scale holes means that the majority of the particles act on the resonance modes in unison, generating clear, mode-dependent resonance shifts and mode-dependent shift polarities which persist up to very high particle coverages. Shifts at intermediate and large particle coverages can be well reproduced via simulation. In contrast to the case of small particles however, the effect of microbeads is analogous to that seen in continuous films with the two major resonance modes both shifting weakly in the same direction. This is due to a lack of particle localization with respect to the spatially periodic nano-scale regions where the modes are localized. Although sub-optimal, detection was nevertheless achieved in such geometries, albeit with low resonance shifts which were similar to those observed in continuous films. Note that the ability to detect particles is determined not only by how sensitive the frequency is to changes in magnetic field but by the ability to generate clear modifications to these frequencies due to favorable particle positioning. A proper choice of particle size and reliable positioning of particles close to well localized modes is thus a critical factor in resonance based sensing.

## V. ACKNOWLEDGMENTS

This research was supported by the Australian Research Council's Discovery Early Career Researcher Award scheme (DE120100155) and Discovery Projects scheme (DP110103980), the United States Air Force (Asian Office of Aerospace Research and Development, AOARD), the University of Western Australia's (UWA) RDA, RCA, ECRFS, SIRF, UPAIS, Re-Entry Fellowship, Teaching Relief and Vacation Scholarship schemes and by resources provided by the Pawsey Supercomputing Centre with funding from the Australian Government and the Government of Western Australia. A.O.A. was supported by the National Research Foundation, Prime Minister's Office, Singapore under its Competitive Research Programme (CRP Award No. NRF-CRP 10-2012-03). The authors thank C. Lueng, M. Albert, W. Wang, A. Suvorova, A. Dodd, C. Yang, D. Schibeci, A. Chew and R.C. Bording for their assistance. The authors acknowledge access to the UWA's Biomagnetics Wet Laboratory and Magnetic Characterisation Facility as well as the facilities, and the scientific and technical assistance of the Australian Microscopy & Microanalysis Research Facility at the Centre for Microscopy, Characterisation & Analysis, The University of Western Australia, a facility funded by the University, State and Commonwealth Governments.

### Appendix A: Additional magnetic particle details

The following particles were used for the sensing experiments. (i) $6 \pm 1$ nm wide iron-oxide nanoparticles (see below); (ii) nanomag-D(-spio) cluster-shaped particles (79-00-501 and 09-00-132; Micromod Partikeltechnologie GmbH) with stated diameters of 50 nm and 130 nm; (iii) 880 nm wide magnetic beads (PMC1N; Bangs Laboratories, Inc.) consisting of iron-oxide nanoparticles within a polymer matrix; and (iv) 4.14 $\mu$m beads (PM-40-10; SpheroTech, Inc.) consisting of a polystyrene core coated with a mixture of polystyrene and magnetic nanoparticles. Concentrations of commercial particle solutions (all aqueous) were determined from the manufacturer's specifications after dilution in purified water. The 6 nm iron-oxide nanoparticles were synthesized under standard Schlenk conditions using the methodology developed by Sun *et al.* [59]. Briefly, $Fe(acac)^3$ (0.7 g, 2 mmol) and 1,2-hexadecanediol (2.5 g, 10 mmol) were dissolved in benzyl ether (20 mL) containing oleylamine (6 mmol) and oleic acid (6 mmol). The resulting mixture was heated at 200 °C

for 2 hours, increased to 260 °C, held for 1 hour then cooled to room temperature. The particles were precipitated by the addition of ethanol (40 mL), centrifuged (5000 rpm, 10 mins) and redispersed in 1,2-dichlorobenzene to the required concentration. These particles have been fully characterized by a range of routine techniques (see Supplementary Figure 10 [57]).

---


[1] D. R. Baselt, G. U. Lee, M. Natesan, S. W. Metzger, P. E. Sheehan, and R. J. Colton, "A biosensor based on magnetoresistance technology", Biosens. Bioelectron. **13**, 731 (1998).

[2] R. S. Gaster, D. A. Hall, C. H. Nielsen, S. J. Osterfeld, H. Yu, K. E. Mach, R. J. Wilson, B. Murmann, J. C. Liao, S. S. Gambhir, *et al.*, "Matrix-insensitive protein assays push the limits of biosensors in medicine", Nat. Med. **15**, 1327 (2009).

[3] H. Lee, T.-H. Shin, J. Cheon, and R. Weissleder, "Recent Developments in Magnetic Diagnostic Systems", Chem. Rev. **115**, 1069010724 (2015).

[4] E. Ng, K. C. Nadeau, and S. X. Wang, "Giant magnetoresistive sensor array for sensitive and specific multiplexed food allergen detection", Biosensors and Bioelectronics **80**, 359365 (2016).

[5] Y. Li, B. Srinivasan, Y. Jing, X. Yao, M. A. Hugger, J.-P. Wang, and C. Xing, "Nanomagnetic Competition Assay for Low-Abundance Protein Biomarker Quantification in Unprocessed Human Sera", J. Am. Chem. Soc. **132**, 4388 (2010).

[6] B. Srinivasan, Y. Li, Y. Jing, C. Xing, J. Slaton, and J.-P. Wang, "A Three-Layer Competition-Based Giant Magnetoresistive Assay for Direct Quantification of Endoglin from Human Urine", Anal. Chem. **83**, 2996 (2011).

[7] C. Duarte, T. Costa, C. Carneiro, R. Soares, A. Jitariu, S. Cardoso, M. Piedade, R. Bexiga, and P. Freitas, "Semi-Quantitative Method for Streptococci Magnetic Detection in Raw Milk", Biosensors **6**, 19 (2016).

[8] Y. R. Chemla, H. L. Grossman, Y. Poon, R. McDermott, R. Stevens, M. D. Alper, and J. Clarke, "Ultrasensitive magnetic biosensor for homogeneous immunoassay", Proc. Natl. Acad. Sci. U.S.A. **97**, 14268 (2000).

[9] P.-A. Besse, G. Boero, M. Demierre, V. Pott, and R. Popovic, "Detection of a single magnetic microbead using a miniaturized silicon Hall sensor", Appl. Phys. Lett. **80**, 4199 (2002).

[10] M. M. Miller, G. A. Prinz, S.-F. Cheng, and S. Bounnak, "Detection of a micron-sized magnetic sphere using a ring-shaped anisotropic magnetoresistance-based sensor: A model for a magnetoresistance-based biosensor", Appl. Phys. Lett. **81**, 2211 (2002).

[11] L. Ejsing, M. F. Hansen, A. K. Menon, H. A. Ferreira, D. L. Graham, and P. P. Freitas, "Magnetic microbead detection using the planar Hall effect", Journal of Magnetism and Magnetic Materials **293**, 677684 (2005).

[12] P. I. Nikitin, P. M. Vetoshko, and T. I. Ksenevich, "New type of biosensor based on magnetic nanoparticle detection", J. Magn. Magn. Mater **311**, 445 (2007).

[13] M. Donolato, M. Gobbi, P. Vavassori, M. Leone, M. Cantoni, V. Metlushko, B. Ilic, M. Zhang, S. X. Wang, and R. Bertacco, "Nanosized corners for trapping and detecting magnetic nanoparticles", Nanotechnol **20**, 385501 (2009).

[14] L. Di Michele, C. Shelly, P. de Marco, P. See, D. Cox, and O. Kazakova, "Detection and susceptibility measurements of a single Dynal bead", J. Appl. Phys. **110**, 063916 (2011).

[15] S. M. Hira, K. Aledealat, K.-S. Chen, M. Field, G. J. Sullivan, P. B. Chase, P. Xiong, S. von Molnár, and G. F. Strouse, "Detection of target ssDNA using a microfabricated Hall magnetometer with correlated optical readout", J. Biomed. Biotechnol. **2012**, 492730 (2012).

[16] J. Devkota, A. Ruiz, P. Mukherjee, H. Srikanth, and M.-H. Phan, "Magneto-Impedance Biosensor With Enhanced Sensitivity for Highly Sensitive Detection of Nanomag-D Beads", IEEE Trans. Magn. **49**, 4060 (2013).

[17] H. J. Chung, C. M. Castro, H. Im, H. Lee, and R. Weissleder, "A magneto-DNA nanoparticle system for rapid detection and phenotyping of bacteria", Nat. Nanotechnol. **8**, 369 (2013).

[18] V. O. Shipunova, M. P. Nikitin, P. I. Nikitin, and S. M. Deyev, "MPQ-cytometry: a magnetism-based method for quantification of nanoparticle–cell interactions", Nanoscale **8**, 12764 (2016).

[19] J. Llandro, T. J. Hayward, D. Morecroft, J. A. C. Bland, F. J. Castano, I. A. Colin, and C. A. Ross, "Quantitative digital detection of magnetic beads using pseudo-spin-valve rings for multiplexed bioassays", Appl. Phys. Lett. **91**, 203904 (2007).

[20] B. Srinivasan, Y. Li, Y. Jing, Y. Xu, X. Yao, C. Xing, and J.-P. Wang, "A Detection System Based on Giant Magnetoresistive Sensors and High-Moment Magnetic Nanoparticles Demonstrates Zeptomole Sensitivity: Potential for Personalized Medicine", Angew. Chem. Int. Ed. **48**, 2764 (2009).

[21] S. J. Osterfeld, H. Yu, R. S. Gaster, S. Caramuta, L. Xu, S.-J. Han, D. A. Hall, R. J. Wilson, S. Sun, R. L. White, and et al., "Multiplex protein assays based on real-time magnetic nanotag sensing", Proc. Natl. Acad. Sci. U.S.A. **105**, 20637 (2008).

[22] D. Hall, R. Gaster, T. Lin, S. Osterfeld, S. Han, B. Murmann, and S. Wang, "GMR biosensor arrays: A system perspective", Biosens. Bioelectron. **25**, 2051 (2010).

[23] P. P. Freitas, F. A. Cardoso, V. C. Martins, S. A. M. Martins, J. Loureiro, J. Amaral, R. C. Chaves, S. Cardoso, L. P. Fonseca, A. M. Sebastião, and et al., "Spintronic platforms for biomedical applications", Lab Chip **12**, 546 (2012).

[24] J.-R. Lee, N. Sato, D. J. B. Bechstein, S. J. Osterfeld, J. Wang, A. W. Gani, D. A. Hall, and S. X. Wang, "Experimental and theoretical investigation of the precise transduction mechanism in giant magnetoresistive biosensors", Scientific Reports **6**, 18692 (2016).

[25] D. Issadore, J. Chung, H. Shao, M. Liong, A. A. Ghazani, C. M. Castro, R. Weissleder, and H. Lee, "Ultrasensitive clinical enumeration of rare cells ex vivo using a micro-hall detector", Science translational medicine **4**, 141ra92 (2012).

[26] P. M. Braganca, B. A. Gurney, B. A. Wilson, J. A. Katine, S. Maat, and J. R. Childress, "Nanoscale magnetic field detection using a spin torque oscillator", Nanotechnol. **21**, 235202 (2010).

[27] R. J. Ryan, H. Xi, and I. Jin, "Magnetic oscillator based biosensor", Patent **US8053244 B2**, (2011).

[28] M. Inoue, A. Baryshev, H. Takagi, P. B. Lim, K. Hatafuku, J. Noda, and K. Togo, "Investigating the use of magnonic crystals as extremely sensitive magnetic field sensors at room temperature", Appl. Phys. Lett. **98**, 132511 (2011).

[29] J. P. Fried and P. J. Metaxas, "Localized magnetic fields enhance the field sensitivity of the gyrotropic resonance frequency of a magnetic vortex", Phys. Rev. B **93**, 064422 (2016).

[30] P. J. Metaxas, M. Sushruth, R. Begley, J. Ding, R. C. Woodward, I. Maksymov, M. Albert, W. Wang, H. Fangohr, A. Adeyeye, and M. Kostylev, "Sensing magnetic nanoparticles using nano-confined ferromagnetic resonances in a magnonic crystal", Appl. Phys. Lett. **106**, 232406 (2015).

[31] M. Albert, M. Beg, D. Chernyshenko, M.-A. Bisotti, R. L. Carey, H. Fangohr, and P. J. Metaxas, "Frequency-based nanoparticle sensing over large field ranges using the ferromagnetic resonances of a magnetic nanodisc", arXiv:1604.07277 - in press @ Nanotechnol. (2016).

[32] K. Mizushima, K. Kudo, T. Nagasawa, and R. Sato, "Signal-to-noise ratios in high-signal-transfer-rate read heads composed of spin-torque oscillators", J. Appl. Phys. **107**, 063904 (2010).

[33] J. R. Petrie, S. Urazhdin, K. A. Wieland, G. A. Fischer, and A. S. Edelstein, "Using a spin torque nano-oscillator to read memory based on the magnetic permeability", J. Phys. D: Appl. Phys. **47**, 055002 (2014).

[34] I. N. Krivorotov, N. C. Emley, J. C. Sankey, S. I. Kiselev, D. C. Ralph, and R. A. Buhrman, "Time-Domain Measurements of Nanomagnet Dynamics Driven by Spin-Transfer Torques", Science **307**, 228 (2005).

[35] H. Suto, T. Nagasawa, K. Kudo, K. Mizushima, and R. Sato, "Real-Time Measurement of Temporal Response of a Spin-Torque Oscillator to Magnetic Pulses", Appl. Phys. Express **4**, 013003 (2010).

[36] Z. Zeng, P. K. Amiri, I. N. Krivorotov, H. Zhao, G. Finocchio, J.-P. Wang, J. A. Katine, Y. Huai, J. Langer, K. Galatsis, *et al.*, "High-power coherent microwave emission from magnetic tunnel Junction nano-oscillators with perpendicular anisotropy", ACS Nano **6**, 6115 (2012).

[37] E. Grimaldi, A. Dussaux, P. Bortolotti, J. Grollier, G. Pillet, A. Fukushima, H. Kubota, K. Yakushiji, S. Yuasa, and V. Cros, "Response to noise of a vortex based spin transfer nano-oscillator", Phys. Rev. B **89**, (2014).

[38] J. Loureiro, R. Ferreira, S. Cardoso, P. P. Freitas, J. Germano, C. Fermon, G. Arrias, M. Pannetier-Lecoeur, F. Rivadulla, and J. Rivas, "Toward a magnetoresistive chip cytometer: Integrated detection of magnetic beads flowing at cm/s velocities in microfluidic channels", Appl. Phys. Lett. **95**, 034104 (2009).

[39] J. Loureiro, P. Z. Andrade, S. Cardoso, C. L. da Silva, J. M. Cabral, and P. P. Freitas, "Spintronic chip cytometer", Appl. Phys. Lett. **109**, 07B311 (2011).

[40] M. Helou, M. Reisbeck, S. F. Tedde, L. Richter, L. Bär, J. J. Bosch, R. H. Stauber, E. Quandt, and O. Hayden, "Time-of-flight magnetic flow cytometry in whole blood with integrated sample preparation", Lab Chip **13**, 1035 (2013).

[41] M. Krawczyk and D. Grundler, "Review and prospects of magnonic crystals and devices with reprogrammable band structure", J. Phys.: Condens. Matter **26**, 123202 (2014).

[42] J. Ding, M. Kostylev, and A. O. Adeyeye, "Magnonic Crystal as a Medium with Tunable Disorder on a Periodical Lattice", Physical Review Letters **107**, (2011).

[43] B. Lenk, H. Ulrichs, F. Garbs, and M. Münzenberg, "The building blocks of magnonics", Physics Reports **507**, 107 (2011).

[44] A. Manzin, G. Barrera, F. Celegato, M. Coïsson, and P. Tiberto, "Influence of lattice defects on the ferromagnetic resonance behaviour of 2D magnonic crystals", Sci. Rep. **6**, 22004 (2016).

[45] H. P. Erickson, "Size and Shape of Protein Molecules at the Nanometer Level Determined by Sedimentation, Gel Filtration, and Electron Microscopy", Biol, Proced. Online **11**, 32 (2009).

[46] L. Li, K. Y. Mak, C. W. Leung, S. M. Ng, Z. Q. Lei, and P. W. T. Pong, "Detection of 10-nm Superparamagnetic Iron Oxide Nanoparticles Using Exchange-Biased GMR Sensors in Wheatstone Bridge", IEEE Transactions on Magnetics **49**, 40564059 (2013).

[47] V. Pospichalova, J. Svoboda, Z. Dave, A. Kotrbova, K. Kaiser, D. Klemova, L. Ilkovics, A. Hampl, I. Crha, E. Jandakova, L. Minar, V. Weinberger, and V. Bryja, "Simplified protocol for flow cytometry analysis of fluorescently labeled exosomes and microvesicles using dedicated flow cytometer", J. Extracell. Vesicles **4**, (2015).

[48] N. Singh, S. Goolaup, and A. O. Adeyeye, "Fabrication of large area nanomagnets", Nanotechnol **15**, 1539 (2004).

[49] I. S. Maksymov and M. Kostylev, "Broadband stripline ferromagnetic resonance spectroscopy of ferromagnetic films, multilayers and nanostructures", Phyica E **69**, 253 (2015).

[50] E. N. Ivanov and M. Kostylev, "Extremely high-resolution measurements of microwave magnetisation dynamics in magnetic thin films and nanostructures", Pre-print: arXiv:1402.3459 [cond-mat.mes-hall] **(vol.: n/a)**, (page: n/a) (2014).

[51] H. Fangohr, G. Bordignon, M. Franchin, A. Knittel, P. A. J. de Groot, and T. Fischbacher, "A new approach to (quasi) periodic boundary conditions in micromagnetics: The macrogeometry", J. Appl. Phys **105**, 07D529 (2009).

[52] A. Vansteenkiste, J. Leliaert, M. Dvornik, M. Helsen, F. Garcia-Sanchez, and B. Van Waeyenberg, "The design and verification of MuMax3", AIP Adv. **4**, 107133 (2014).

[53] J. D. Hunter, "Matplotlib: A 2D graphics environment", Comput. Sci. Eng. **9**, 90 (2007).

[54] S. van der Walt, S. C. Colbert, and G. Varoquaux, "The NumPy Array: A Structure for Efficient Numerical Computation", Comp. Sci. Eng. **13**, 22 (2011).

[55] P. J. Metaxas, M. Albert, S. Lequeux, V. Cros, J. Grollier, P. Bortolotti, A. Anane, and H. Fangohr, "Resonant translational, breathing, and twisting modes of transverse magnetic domain walls pinned at notches", Phys. Rev. B **93**, 054414 (2016).

[56] T. Fischbacher, M. Franchin, G. Bordignon, and H. Fangohr, "A Systematic Approach to Multiphysics Extensions of Finite-Element-Based Micromagnetic Simulations: Nmag", IEEE Trans. Mag. **43**, 2896 (2007).

[57] See Supplemental Material at [URL will be inserted by publisher] for additional data.

[58] J. Ding, N. Singh, M. Kostylev, and A. O. Adeyeye, "Static and dynamic magnetic properties of $Ni_{80}Fe_{20}$ anti-ring nanostructures", Phys. Rev. B **88**, 014301 (2013).

[59] S. Sun, H. Zeng, D. B. Robinson, S. Raoux, P. M. Rice, S. X. Wang, and G. Li, "Monodisperse $MFe_2O_4$ (M = Fe, Co, Mn) Nanoparticles", J. Am. Chem. Soc. **126**, 273 (2004).